Vibrations and thermal transport in nanocrystalline silicon

Arun Bodapati,[1,*] Patrick K. Schelling,[2] Simon R. Phillpot,[3] and Pawel Keblinski[1,†]

[1]*Department of Materials Science and Engineering, Rensselaer Polytechnic Institute, Troy, New York 12180, USA*
[2]*Advanced Materials Processing and Analysis Center (AMPAC) and Department of Physics, University of Central Florida, Orlando, Florida 32816, USA*
[3]*Department of Materials Science and Engineering, University of Florida, Gainesville, Florida 32611, USA*

We use a combination of vibrational-mode analysis and molecular-dynamics simulations to study the effect of grain size on the nature of thermal vibrations, their localization, and their ability to carry heat in nanocrystalline silicon. Vibrational-mode analysis demonstrates that the vibrations that carry most of the heat in small-grain ($\lesssim 3$ nm) structurally heterogeneous nanocrystalline silicon are almost identical in nature to those in homogeneous amorphous silicon, where the majority of the vibrations are delocalized and unpolarized. Consequently, the principal thermal conductivity mechanism in such a nanocrystalline material is the same as in the amorphous material. With increasing grain size, the vibrational modes become progressively more like that of a crystalline material; this is reflected in a crossover in the mechanism of thermal transport to that of a crystalline material.

PACS number(s): 65.80.+n

I. INTRODUCTION

A fundamental understanding of thermal transport mechanisms in nanocrystalline materials is of importance for various practical applications: polycrystalline and nanocrystalline silicon play a central role in modern integrated circuits,[1,2] nanocrystalline diamond has the potential for thermal management in sensitive microelectronic devices,[3] nanocrystalline Re-Si (Ref. [4]) composites and SiGe are interesting thermoelectrics,[5] and polycrystalline yttria-stabilized zirconia (YSZ) is a thermal barrier coating.[6] In each case the performance and reliability depend upon the heat transfer properties.

As the grain size of nanocrystalline materials is reduced below a critical limit, they become thermodynamically unstable with respect to their amorphous counterpart and a phase transition between the nanocrystalline and amorphous phases can occur.[7,8] Within this context, we address the nature of the accompanying transition in the vibrational behavior of nanocrystalline materials from that characteristic of crystalline materials to that characteristic of amorphous materials. Furthermore, this transition should have a signature in thermal transport behavior.

Using an approach that combines phonon analysis and molecular-dynamics (MD) simulations of heat flow in model nanocrystalline silicon structures, we expose the transition in thermal transport mechanism from amorphous like to crystalline like and demonstrate that it is to a large extent independent of the structural transition. Our vibrational analysis demonstrates that this behavior originates from the "amorphous" nature of vibrations that dominate thermal transport in small-grain-size nanocrystals. Only for larger-grain-sized nanocrystals is the majority of the heat carried by vibrations with the well-defined polarizations and wave vectors characteristic of crystalline materials.

The rest of the paper is organized as follows: We present a brief background on thermal transport in polycrystalline and amorphous solids in Sec. II. In Sec. III we describe the model structures used in this study and the MD methodology used to determine the thermal conductivity of the structures. In Sec. IV, we present an analysis of the vibrational properties of various model nanocrystalline structures. In Sec. V, we present and discuss our results from MD simulations. The summary and conclusions are presented in the last section. A brief report of parts of this work has appeared elsewhere.[9]

II. BACKGROUND ON THERMAL TRANSPORT

The total area of grain boundaries (GB's), and hence the excess energy of a nanocrystalline or polycrystalline material, increases as the inverse of the grain size. Since GB's make a significant contribution to the energy of a polycrystal, as the grain size of a nanocrystalline material is reduced, a competition develops between the tendency to remain nanocrystalline, on the one hand, and the tendency to form an amorphous phase, on the other. To address the vibrational properties and thermal transport properties of small-sized nanocrystalline materials, it is therefore imperative that we understand the vibrational properties and thermal transport mechanisms of both polycrystalline and amorphous materials.

A general understanding of atomic vibrations or phonon-mediated thermal transport in crystalline solids, including their dependence on temperature, defect concentration, and grain size, is provided by the Klemens-Callaway (KC) model.[10,11] In this model heat is carried by quanta of propagating and polarized vibrational modes (i.e., phonons). The actual value of the thermal conductivity is governed by the heat capacity, phonon group velocity (the speed of sound), and their mean free path between scattering events (or alternately their relaxation time). The central assumption of the KC model is that that all phonon scattering processes, such as those related to point defects, grain boundaries, or phonon-phonon scattering, are independent of each other and can be represented simply by characteristic relaxation times which are functions of frequency ω and temperature T. Fur-

thermore, the KC model assumes a Debye spectrum. Consequently, the temperature-dependent thermal conductivity κ is given as[12,13]

$$\kappa = \frac{1}{2\pi^2 v} \left(\frac{k_B T}{\hbar} \right)^3 \int_0^{\Theta_D/T} x^2 \tau(x) C(x) dx, \qquad (1)$$

where $x = \hbar\omega/k_B T$, with $\hbar$ and k_B denoting Planck's and Boltzmann's constants, respectively, v is the speed of sound in the material, $\tau(x)$ is phonon relaxation time, $C(x)$ is the phonon specific heat, and Θ_D is the Debye temperature. Within the KC model, κ can be estimated from the combined relaxation time τ_c, which is the sum of reciprocals of relaxation times of momentum conservative normal (N) processes and nonconservative phonon scattering processes such as umklapp (U) processes, and for point defect (P) and boundary scattering (GB):

$$\tau_c^{-1} = \tau_N^{-1} + \tau_U^{-1} + \tau_p^{-1} + \tau_{GB}^{-1}. \qquad (2)$$

The relaxation time due to grain boundary scattering, τ_{GB}, is usually assumed to be frequency independent and equal to L/v, where L is the grain size and v is the speed of sound in the material. The relaxation times for the remaining scattering processes can be found in detail elsewhere.[12,13]

A general conclusion of the KC model[13] is that well below the Debye temperature Θ_D, the thermal conductivity in coarse-grained polycrystalline materials increases with temperature as $\kappa \propto T^3$, essentially following the quantum-mechanical formula for the temperature dependence of the phonon contribution to the specific heat. In this temperature regime the scattering is controlled by grain boundaries and surfaces. At higher temperatures resistance to thermal transport is primarily offered by momentum nonconservative umklapp processes leading to a decrease in κ of polycrystalline materials with increasing temperature as $\kappa \propto (1/T)^\alpha$, with the numerical value of α depending upon the chemistry of the material.[12] In materials with very small grain sizes, phonons are much more likely to scatter from a grain boundary before they can scatter from other phonons; thus, in nanocrystalline materials, the scattering even at high temperature is dominated by GB's, leading to a thermal conductivity that is strongly dependent on the grain size.

The thermal transport mechanisms in amorphous materials are qualitatively different from those in crystalline and polycrystalline solids. As a result of the high degree of structural disorder, the idea of propagating and polarized phonons is no longer meaningful. As a consequence of their inability to support propagating phonons, the thermal conductivities of amorphous solids are greatly reduced relative to that of their crystalline counterparts. Furthermore, the temperature dependence of thermal conductivity, $\kappa(T)$, for a variety of glasses[14] consists of three regimes: (i) at low temperatures ($T < 10$ K), where only low-energy vibrations are excited, $\kappa \propto T^2$, compared with the T^3 dependence in crystalline materials. This behavior was explained by Anderson *et al.* and independently by Phillips as resonant scattering by tunneling states in a two-level system,[15,16] although this point is not entirely without controversy. (ii) At slightly higher temperatures[17] (10–30 K), the thermal conductivity is essen-

tially temperature independent, exhibiting a plateau. (iii) Above this, thermal conductivity increases slowly with temperature and saturates to a temperature-independent value.

From studies of the vibrational modes of amorphous silicon within the harmonic approximation, Feldman and co-workers[17,18] developed an understanding of the latter two temperature regimes. In this context vibrations in glasses were classified as[19] (i) *propagons*, low-frequency vibrations, similar to phonons: they can be described by a wave vector, are polarized, and propagate as waves; however, they constitute only ~4% of the total modes of amorphous silicon; (ii) *diffusons*, which cannot be described by a wave vector, are unpolarized, and transport energy diffusively, these constitute ~93% of the total modes; and (iii) *locons*, or high-frequency localized modes constituting only about ~3% of the total modes.

Using this description of vibrational modes, Feldman *et al.* successfully explained the high-temperature behavior of κ of amorphous silicon within the harmonic approximation,[17] wherein thermal energy is primarily transported by *diffusons*.[18]

In the above context the key question we address in this work is, in nanocrystalline materials, is heat carried by propagating phonons that scatter at grain boundaries, as is the case in polycrystals, or by a mechanism more typical of amorphous materials? We anticipate that the transition from crystalline to amorphous thermal transport properties need not coincide with the analogous structural transition because the crystalline phonon-mediated thermal transport might become inoperative when the wavelength of heat-carrying phonons is comparable with the grain size, a size that is generally well above the grain size for the structural transition.

III. MODEL STRUCTURES AND SIMULATION METHODOLOGY

A. Model structures

To represent the key feature of structural heterogeneity we chose one-dimensional periodic superlattices of silicon grain boundaries as the primary model structures. Atomic interactions are described by the Stillinger-Weber potential.[20] As a representative GB, we selected a (001) $\theta = 43.60°$ $\Sigma 29$ twist GB, which is a high-angle, high-energy twist grain boundary on the (001) plane (see Fig. 1), thought to be representative of those in polycrystalline materials.[21] Due to the computational demands of the vibrational mode analysis, our model GB structures contained just two identical grains misoriented by a twist along the z direction separated by two GB's. Periodic boundary conditions were used in all three directions, consequently leading to planar GB's. The simulation cells containing the GB superlattices had a cross-sectional area of 2.1×2.1 nm². With the cross-sectional area of the x-y plane kept constant, different unit cells were generated with different GB spacings, representing different grain sizes, d_z, varying from 1.6 to 10.8 nm, with the total number of atoms ranging from 696 to 4640, respectively.

To assess the role of the GB structure and energy we also studied the $\Sigma 31$ GB which is a low-energy, high-angle twist
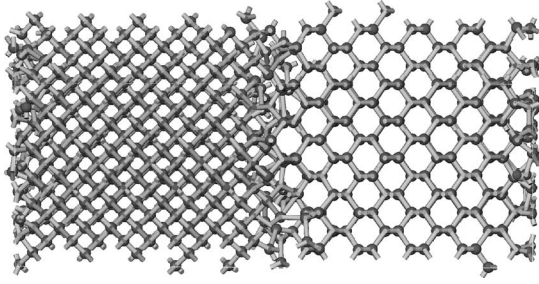
FIG. 1. Atomic positions and bonding in a high-angle (001) $\Sigma 29$ twist grain boundary in silicon with GB separation $d_z = 2.7$ nm. Two grains are separated by two GB's, one at the center and one at the edges of the simulation box. Periodic boundary conditions are used in all three directions.

GB on the (111) plane (which is the most dense plane in the diamond lattice). This GB has energy which is about half that of (001) Σ 29 GB and exhibits a much larger degree of structural order.

To address the finite-size effects in the MD simulations, we used GB superlattices consisting of 12 grains separated by 12 crystallographically identical GB's. These structures were generated by repeating 6 unit cells along the z direction of the (001) GB structures described in the previous paragraph. Also in this case, the simulation cells were periodic in all three directions with a cross section of 2.1×2.1 nm^2 and the grain boundary spacing d_z ranging from 1.6 to 10.8 nm, with the corresponding total number of atoms ranging from 4176 to 27840.

To probe a degree of structural complexity not present in the planar GB superlattices, we also calculated the thermal conductivity of fully textured two-dimensional (2D) microstructures consisting of columnar grains, each aligned with [001] along the texture direction (z in this case), but randomly oriented in the plane (x-y) of the film. As a result of this, all of the grains are (001) tilt grain boundaries. Five geometrically equivalent model structures with grain sizes ranging from ∼2 to 6.5 nm with the corresponding total number of atoms ranging from 9534 to 114 786 were generated and analyzed.

B. Molecular-dynamics simulations

Each of the structures used in the vibrational analysis was first annealed by MD simulations at $T = 1350$ K (80% of the melting point of silicon, of $T_{m,\text{Si}} = 1687$ K, which is very closely reproduced by the Stillinger-Weber potential[22]) for 2×10^6 MD time steps of 0.55 fs each, then quenched, and finally relaxed to $T = 0$ K and zero pressure. Structures used in the MD simulations were quenched to 300 K and then equilibrated prior to the thermal conductivity simulations described below. A more detailed description of the generation of GB structures can be found in a previous study by Keblinski *et al.*[23]

To compute the thermal conductivity by MD simulations, we used a methodology which is analogous to experiment. The basic idea was to generate a steady-state heat current across the system, determine the associated temperature gra-

dient, and then use Fourier's law to determine thermal conductivity κ. Figure 2 shows a schematic representation of the simulation cell used to compute κ. After equilibrating each structure at $T = 300$ K, at each MD time step, atomic velocities were rescaled to add heat $\Delta\epsilon$ in a thin slab of thickness δ centered at $z = -L/4$ (*hot source*) and removed from a slab of the same thickness at $z = +L/4$ (*cold sink*). Due to this setup of a heat source and sink, a constant heat flux $J_z = \frac{\Delta\epsilon}{2A\Delta t}$ was established, where A is the cross-sectional area of the simulation cell in the x-y plane and Δt is the MD time step. The factor of 2 in the denominator of the heat flux is due to the fact that half the heat flows to the right and half to the left of the heat source and sink (see Fig. 2). The temperature profile across the cell was calculated from the kinetic energies of atoms in slices along the z direction averaged over 3.5×10^6 MD steps of 0.55 fs each. Before collecting the temperature profiles, the system was simulated for 1.5×10^6 MD steps to allow the system to achieve a steady-state temperature profile. The temperature gradient $\partial T/\partial z$ was obtained from a linear fit to the temperature versus position plots. With knowledge of the temperature gradient and the amount of heat flux, the thermal conductivity κ was estimated using Fourier's law:

$$\kappa = -\frac{J_z}{\partial T/\partial z}. \tag{3}$$

To eliminate the tendency of center of mass of the system to drift, which would result in an erroneous temperature profile, we used the modified velocity-rescaling algorithm of Jund and Jullien.[24] Further, to establish that Fourier's law is obeyed and eliminate the effect of $\Delta\epsilon/A$ on the value of κ calculated, we used a value of $\Delta\epsilon/A = 1.06 \times 10^{-4}$ eV/nm^2, which has been shown in previous simulations of bulk crystalline silicon[25] to give reasonably accurate values of κ. As equal amounts of kinetic energy were being added and removed, the total energy in our simulations was well conserved over entire simulation runs.

The MD simulation method described above, also known as the direct method,[26] has been systematically compared with the indirect methods based on Green-Kubo formalism by Schelling *et al.* in a previous study.[25] It has also previously been argued[27] that the Green-Kubo methods were inappropriate for inhomogeneous systems such as those consisting of grain boundaries and that a direct method such as setting up a heat source and sink must be used, which is the case in the present study.

C. Vibrational-mode calculations

We performed a standard real-space mode analysis by assuming that the normal-mode solution takes the form of $u_{i\alpha\lambda} = (1/\sqrt{m_i})\varepsilon_{i\alpha,\lambda}\exp(i\omega_\lambda t)$. To find the normal-mode eigenfrequencies ω_λ and their corresponding eigenvector components $\varepsilon_{i\alpha,\lambda}$, we solved the lattice dynamical equation

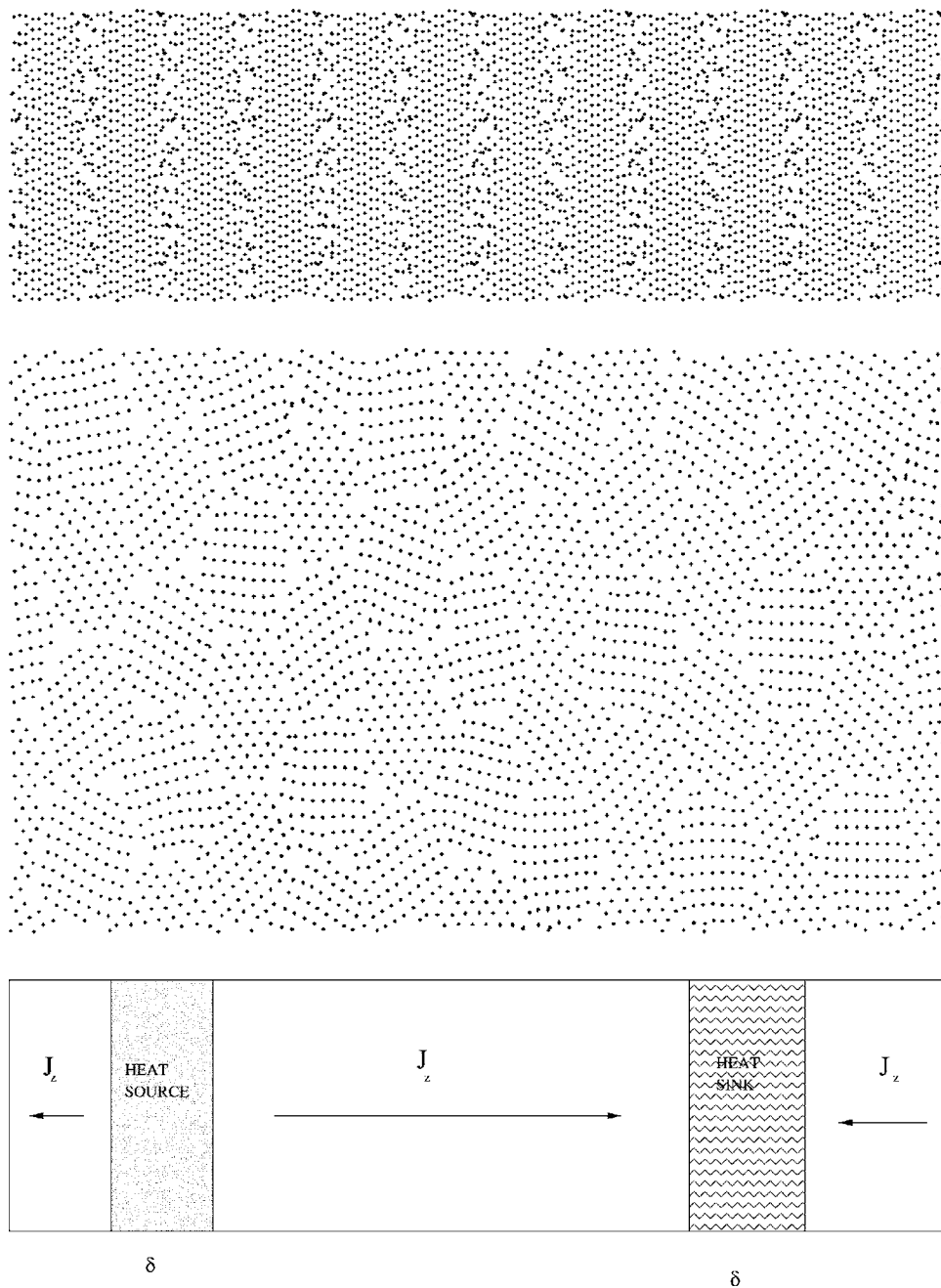$$\omega_\lambda^2 \varepsilon_{i\alpha,\lambda} = \sum_{j\beta} \Phi_{i\alpha,j\beta}\varepsilon_{j\beta,\lambda}, \tag{4}$$

FIG. 2. *Bottom panel:* schematic of three-dimensional periodic simulation cell for estimation of κ_{MD} using MD simulations. Both the source and sink are slabs of equal thickness δ wherein, at each time step, energy $\Delta\epsilon$ is added and removed, respectively. Top panels show atomic structures corresponding to 1D GB superlattices and 2D textured columnar microstructures.

where the elements of the matrix Φ are given as

$$\Phi_{i\alpha,j\beta} = \frac{1}{\sqrt{m_i m_j}} \frac{\partial^2 V}{\partial u_{i\alpha} \partial u_{j\beta}}. \tag{5}$$

Here $u_{i\alpha}$ is the displacement of ion i in the α Cartesian direction, m_i is the mass of ion i, and V is the total potential energy. The reduced force constant matrix was calculated numerically using a finite-difference approach involving very small atomic displacements. The normal modes of our model GB structures with N atoms were calculated by diagonalizing

the $3N \times 3N$ matrix given by Eq. (5). We would like to note that the computational load of diagonalizing large matrices limited the largest grain size in our vibrational analysis to 5.4 nm, which corresponds to $N = 2320$.

The thermal conductivity can be computed from the vibrational modes by applying the Allen-Feldman (AF) theory of disordered solids within the harmonic approximation.[17,18] As described in Sec. II, this theory is applicable to disordered systems where the majority of vibrations are delocalized yet unpolarized (e.g., amorphous silicon). Within this theory, thermal conductivity is given by[18]

$$\kappa_{AF} = \frac{1}{V}\sum_\lambda c_\lambda(T)D_\lambda, \tag{6}$$

where V is the volume and $c_\lambda(T)$ and D_λ are the mode-dependent heat capacity and mode diffusivity, respectively. The mode diffusivity given by[18]

$$D_\lambda = \frac{\pi V^2}{3\hbar^2\omega_\lambda^2}\sum_{\lambda\neq\mu}|\mathbf{S}_{\lambda\mu}|^2\delta(\omega_\lambda - \omega_\mu) \tag{7}$$

is a temperature-independent quantity which is estimated from the heat current operator $\mathbf{S}_{\lambda\mu}$ within the harmonic approximation.[18] To compute the mode diffusivity D_λ from Eq. (7) for a finite system such as our GB structures, which in principle has discrete eigenfrequencies, we used a Lorentzian of width 0.13 rad THz to mimic a broadened δ function with a width greater than the level spacings. We would like to clarify that the unit rad THz is simply to indicate a factor of 2π in the width of the Lorentzian. All of our calculations in the present work were done with this width. Further increasing the width of the Lorentzian by $\sim 15\%$ increased the thermal conductivity estimate by $<1\%$; however, it increased the computation time by almost twofold. In our study of GB structures, we computed the component of mode diffusivities and the corresponding thermal conductivity along the (z) direction normal to the GB plane which is in the x-y plane. As a result, our calculations are limited to determining the effective thermal conductivity perpendicular to the grain boundaries. Transport parallel to the grain boundary interfaces was not considered.

IV. VIBRATIONAL MODE ANALYSIS

In this section, we present an analysis of vibrational properties of nanocrystalline structures. We performed a vibrational-mode analysis on each of our unit cells of GB structures including high-energy (001) GB's with spacings d_z ranging from 1.6 to 5.4 nm and one low-energy (111) GB with 2.7 nm GB separation.

A. Local vibrational density of states

The first important characteristic of the vibrational properties is the vibrational density of states (VDOS) which measures number of vibrations within a given frequency range. Considering that our structures are highly inhomogenous, it is useful to examine the relative contribution of atoms in the grain boundaries to the total VDOS. Following Feldman and Bernstein,[28] the local vibrational density of states, $g_{j'}$ is defined as

$$g_{j'}(\omega) = \sum_j{}'\sum_\lambda\sum_\alpha(\varepsilon_{j\alpha,\lambda})^2\delta(\omega - \omega_\lambda), \tag{8}$$

where ω_λ is the frequency of vibrational mode λ. The prime denotes that the sum over j includes atoms either within ~ 1-nm slabs containing the grain boundary or the rest of the system—i.e., grain interiors. The sum of the local VDOS for GB's and grain interiors gives the total VDOS.
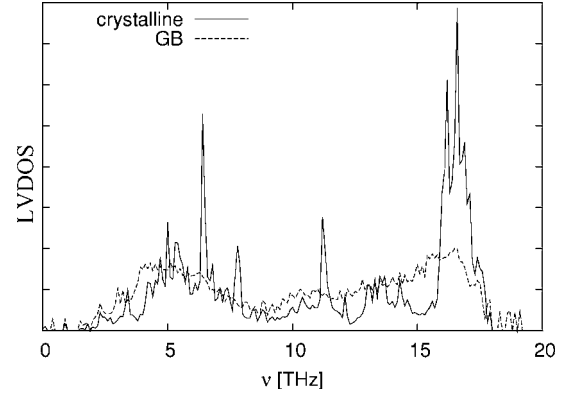

FIG. 3. Local GB and grain interior vibrational DOS as a function of frequency for GB structure with $d_z=2.7$ nm.

Figure 3 shows the local VDOS for the GB's and crystalline grain interiors for the GB structure with $d_z=2.7$ nm. Very similar results were obtained for other GB separations. The two local VDOS are quite distinct, particularly in the high-frequency optical phonon region (~ 16 THz). In fact, the crystalline grain interiors exhibit a local vibrational density of states akin to that of bulk silicon, while the local VDOS at GB's are akin to that of amorphous silicon. Similar behavior was observed in recent studies of amorphous/crystalline silicon sandwich structures[28] and in studies of nanocrystalline metals.[29] Therefore, the analysis of the VDOS suggests that vibrational properties of the nanocrystalline silicon can be simply understood in terms of a two-phase structural model involving crystalline grain interiors and more or less disordered GB's. However, we will demonstrate below that the detailed picture is much more subtle and is exemplified by the transition in the thermal transport characteristics.

B. Mode localization

The VDOS and local VDOS provide information averaged over all vibration modes present in the structure. By contrast, the participation ratio p_λ, defined for each mode λ as[19,30,31]

$$p_\lambda^{-1} = N\sum_i\left(\sum_\alpha\varepsilon_{i\alpha,\lambda}^*\varepsilon_{i\alpha,\lambda}\right)^2, \tag{9}$$

where $\varepsilon_{i\alpha,\lambda}$ is the vibrational eigenvector component, characterizes each mode individually and serves as a useful discriminant of spatial localization. The participation ratio measures the fraction of atoms participating in a mode and hence varies between $O(1)$ for delocalized states to $O(1/N)$ for localized states and effectively indicates the fraction of atoms participating in a given mode.

Figure 4 compares the participation ratios of all modes in the spectrum for the perfect crystal, the amorphous phase, (001) GB structures with grain sizes of $d_z=2.7$ nm, $d_z=5.4$ nm, and the (111) GB structure with $d_z=2.7$ nm. In the perfect crystal, the participation ratios range from about 0.5 to almost 1, characterizing extended modes in which most of the atoms participate. Most of the modes in the GB structures
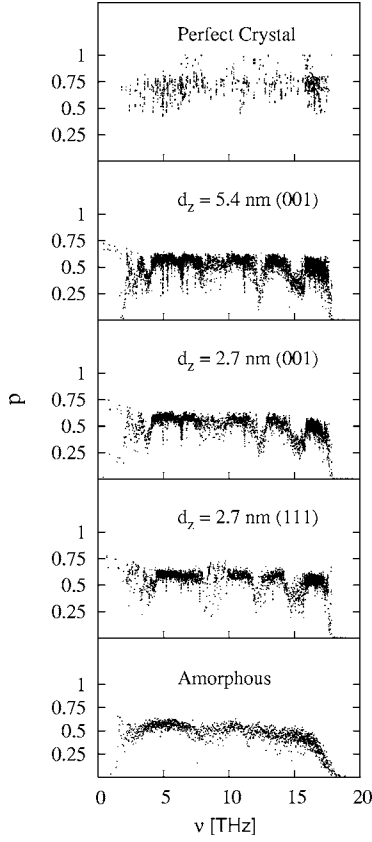
FIG. 4. Participation ratio vs frequency for amorphous silicon, (111) GB structure with $d_z = 2.7$ nm, (001) GB structures with $d_z = 2.7, 5.4$ nm, and perfect crystal structure of silicon.
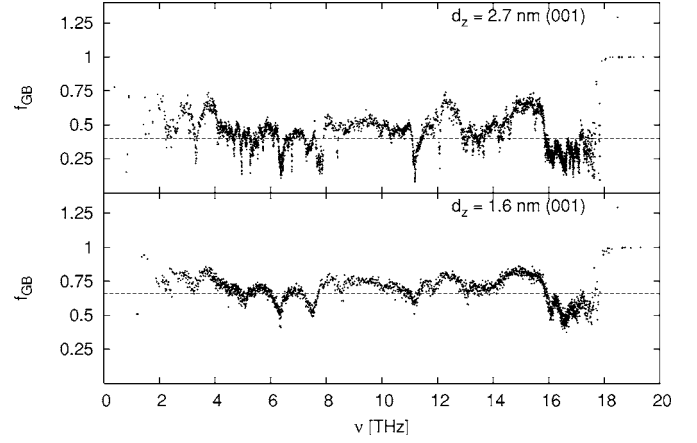

FIG. 5. Fraction of each mode contained in the grain-boundary region of the GB structure. Mode weight factor as a function of frequency for (001) GB model structure with (*top panel*): $d_z = 2.7$ nm and (*bottom panel*): $d_z = 1.6$ nm. The dashed lines at 0.66 (bottom panel) and 0.4 (top panel) mark the volume fraction of GB region in the structure with $d_z = 1.6$ nm and 2.7 nm, respectively.

$$f_{j',\lambda} = \sum_j {}' \sum_\alpha (\varepsilon_{j\alpha,\lambda})^2, \tag{10}$$

where the prime denotes that the sum over j (atoms) is alternately restricted to the crystalline interior or the grain-boundary interface, and consequently the mode weight factors in our GB structures are complementary to each other—i.e., $f_{crys,\lambda} + f_{GB,\lambda} = 1$. As $f_{GB,\lambda} \to 1$ (or $f_{crys,\lambda} \to 0$), the mode λ tends to become more localized on the grain boundary.

In Fig. 5 we show f_{GB} as a function of frequency for 2.7- and 1.6-nm (001) GB structures. We first note that in the low- and intermediate-frequency regions f_{GB} is more or less equal to the volume fraction of the GB regions (see dashed lines in Fig. 5), again demonstrating that these modes are delocalized and equally distributed over GB's and grain interiors. In the optical region (~ 16 THz), the fractional contribution at the GB's is smaller as these modes are largely confined to the grain interiors. The modes forming the high-frequency end ($\gtrsim 18$ THz) are completely localized at the GB. These modes can be thought of as vibrations localized on some over coordinated regions that form a stiffer environment. It is natural that such modes cannot be supported in the perfectly coordinated grain interiors.

It is also evident from Fig. 5 and consistent with Fig. 4 that there are a number of modes in the low- and intermediate-frequency regions which are predominantly weighted either to GB's or to grain interiors. Examples of such modes are illustrated by Fig. 6, which shows the amplitude of atomic displacement as function of z coordinate for two selected modes. The first mode with frequency ~ 11 THz is more active in grain interiors, while the second (~ 12 THz) is more of a GB interface mode. We note that neither mode is strictly localized to a single GB interface or grain interior but instead is active either in both GB interfaces or both grain interiors, leading to the interpretation that these modes are resonant modes[19] rather than localized modes.

have participation ratio of ~ 0.5–0.6, which is similar to amorphous silicon and characteristic of delocalized modes. However, in the optical frequency region of ~ 16 THz the participation ratio is much lower, as those modes tends to be localized more in the crystalline grain interiors, which is consistent with local VDOS results shown in Fig. 3.

Furthermore; the GB structures also have a number of high-frequency modes ($\nu > 18$ THz) with very low participation ratio that corresponds to modes localized within clusters of atoms residing near the GB interface. These modes are analogous to the localized high-frequency modes, locons,[19] observed in amorphous silicon. There are also a number of modes at intermediate frequencies with relatively low participation ratios (see Fig. 4). Examination of the corresponding eigenmodes shows that these modes are either confined to GB interfaces or alternately the grain interiors. The localized modes are discussed later in more detail. Interestingly, the participation ratios for (001) and (111) GB structures with $d_z = 2.7$ nm are very similar (see Fig. 4), despite their differences in GB energy and structure.

Although the participation ratio p_λ indicates the spatial extension over the entire GB structure, it does not provide information about the relative contributions of individual modes from crystalline and grain-boundary regions of the GB structure. This regional contribution of modes can be characterized by the mode weight factor defined as[28]
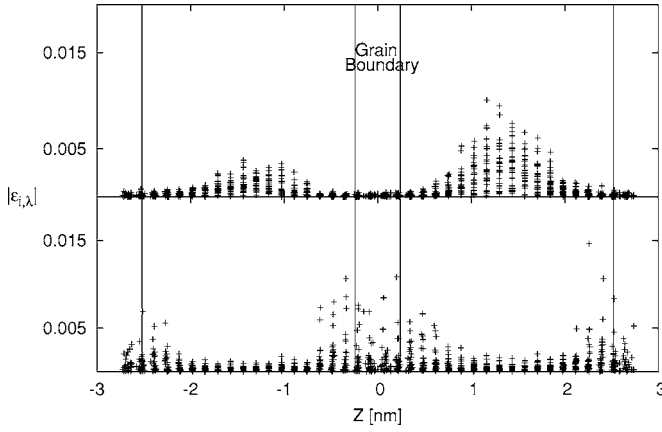
FIG. 6. Spatial variation of amplitude of a mode projected along the z direction. The region between the vertical lines as shown is the region of grain boundary in (001) GB structure with $d_z=2.7$ nm. Top panel: $\nu \sim 11$ THz, *localized* in grain interiors. Bottom panel: $\nu \sim 12$ THz, localized on grain boundaries.

C. Polarization of modes

While the participation ratios reveal that the majority of modes in the crystalline, nanocrystalline, and amorphous structures are delocalized, the polarization characteristics are dramatically different in the different structures. These differences were elucidated by examining the Cartesian components of unit polarization vectors $e_{i\alpha,\lambda}$, of an atom i, for a given mode λ, defined as[30]

$$e_{i\alpha,\lambda} = \frac{\varepsilon_{i\alpha,\lambda}}{\sum_{\alpha} \varepsilon_{i\alpha,\lambda}^* \varepsilon_{i\alpha,\lambda}}. \quad (11)$$

In a crystal without defects, the normal modes are all phonon modes and possess well-defined polarization vectors. For example, for an LA mode, if the polarization vector is parallel to $\mathbf{k}$ (say, the z direction), then each ion has a unit polarization vector component of ± 1 in the z direction and 0 in the x and y directions (see Fig. 7).

Figure 7 shows the projection of the sphere of normalized unit polarization vectors onto the x-z and y-z planes forming circles for a typical mode at about a frequency of 3 THz, for crystalline, (001) GB with $d_z=5.4$ nm, (001) GB with $d_z=2.7$ nm, and amorphous structures. Each point in the circle represents a Cartesian component α of a unit polarization vector $e_{i\alpha,\lambda}$ corresponding to an atom i for the given mode λ. For the amorphous structure, the atomic displacements are uncorrelated and fill the circle more or less uniformly. This depolarized nature is also characteristic of the mode in the $d_z=2.7$ nm (001) GB structure. There is, however, a small degree of preference along the z direction in the polarization circle of the GB structures which is more pronounced for $d_z=5.4$ nm (001) GB structure. This clearly indicates that with increasing grain separation, the modes begin to acquire a longer polarization memory, characteristic of phonons in a crystalline structure with a well-defined polarization (see top panel in Fig. 7).
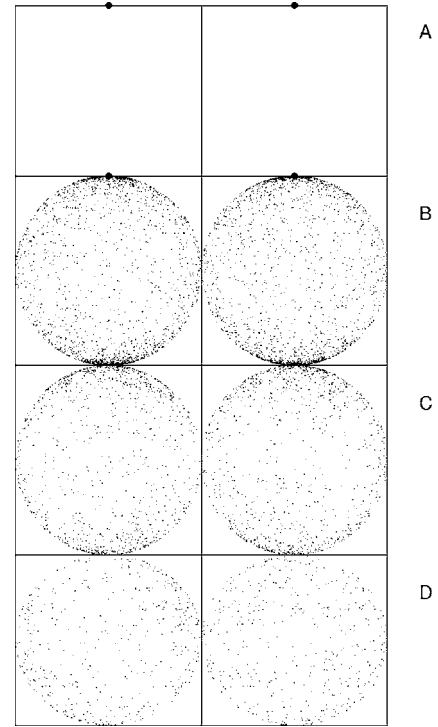

FIG. 7. Projection of normalized unit polarization vector components z vs x (left-hand column) and z vs y (right-hand column) for (A) crystalline silicon, (B) (001) GB with $d_z=5.4$ nm, (C) (001) GB with $d_z=2.7$ nm, and (D) amorphous silicon. Each of the polarization vectors plotted here is characteristic for a mode with a participation ratios $p_\lambda \sim 0.5$ and frequency $\nu_\lambda \sim 3$ THz in the respective structures.

D. Phase quotient

The phase quotient Φ_λ, of a mode λ, defined as[19]

$$\Phi_\lambda = \frac{\sum_{\langle i,j \rangle} \left(\sum_{\alpha} \varepsilon_{i\alpha,\lambda} \varepsilon_{j\alpha,\lambda} \right)}{\sum_{\langle i,j \rangle} \left| \sum_{\alpha} \varepsilon_{i\alpha,\lambda} \varepsilon_{j\alpha,\lambda} \right|}, \quad (12)$$

where i and j are nearest neighbors, is a discriminant of the acoustic versus optical nature of the mode. A value of $\Phi_\lambda \rightarrow 1$ indicates that nearest-neighbor atoms vibrate mostly in-phase like an acoustic mode while values near -1 indicate that they vibrate out of phase in a manner characteristic of an optical mode.

Figure 8 shows the phase quotient as a function of frequency for amorphous, GB structures, with $d_z=1.6$ and 2.7 nm, and crystalline silicon. Due to a lack of well-defined polarization, *diffusons* in amorphous silicon are identical in any small frequency window and this is reflected in their phase quotients, which form a band of monotonically decreasing values is observed. However, there is an increase of phase quotient in the 7–9-Thz range. As Allen *et al.*[19] pointed out, in amorphous silicon this increase coincides with the end of the transverse acoustic TA branch in crystalline silicon at approximately 8 THz. As the TA branch ends, the modes begin to acquire features akin to LA, leading to an increase in the phase quotient. This in contrast to crystalline
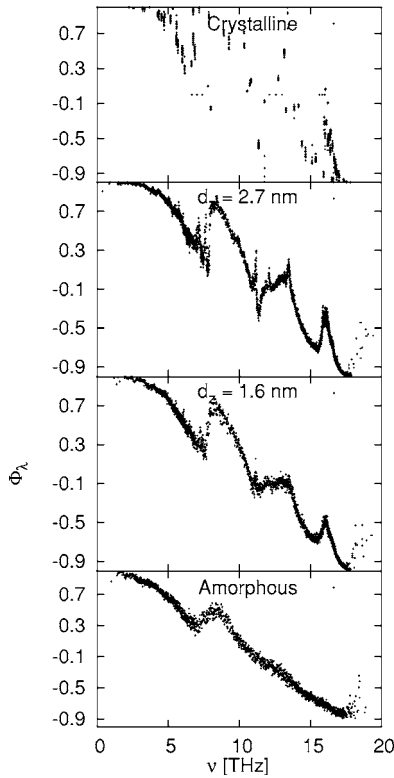
FIG. 8. Mode phase quotients as a function of frequency for crystalline, (001) GB with d_z=2.7 nm, 1.6 nm, and amorphous silicon.

FIG. 9. Mode diffusivities as a function of frequency for (001) GB with d_z=2.7 nm, 1.6 nm, and amorphous silicon. An increase in grain size leads to an increase in mode diffusivity across the spectrum.

silicon where the phase quotients of the modes do not form a band as they retain their individual idiosyncratic vibrational character with a well-defined polarization across the spectrum.

Consistent with our prior analysis, the frequency dependence of the phase quotient is similar to that of amorphous silicon; with increasing grain size, the phase quotient of the vibrational modes across the spectrum gradually acquires features characterizing crystalline silicon.

The counterintuitive idea that emerges from this analysis of the vibrational properties of the GB structures is that despite the structural order present in the nanocrystals, the majority of their vibrations are similar in spatial extension and polarity to the vibrational modes of the amorphous structures. Additionally, we find that the vibrational properties change quite smoothly from amorphous like to crystalline like with increasing grain size. These trends immediately raise the question of how this affects the ability of these vibrational modes to transport thermal energy.

V. THERMAL CONDUCTIVITY

In the previous section, we demonstrated the close similarity in the nature of the atomic vibrations between small-grain-sized nanocrystalline silicon and amorphous silicon. In this section, we identify the consequences of these similarities on thermal transport mechanisms in nanocrystalline silicon. To do this, the thermal conductivity was computed by two independent methods, (i) the direct MD simulation
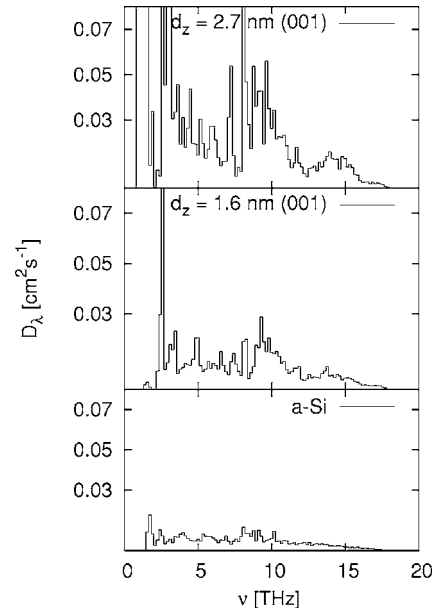
method and (ii) the mode diffusivities and the Allen-Feldman theory of disordered solids within the harmonic approximation,[17,18] as described in Sec. III.

Figure 9 shows the mode diffusivities, which measure the contribution of each mode to the thermal conductivity using Eq. (6) of the amorphous phase and of (001) GB structures with d_z=1.6 and 2.7 nm. Clearly, the diffusivities of the modes increase with increasing grain size. As is expected, the optical modes, which are localized largely in the grain interiors, have low diffusivities. Therefore, while these modes contribute to the vibrational density of states and to the participation ratio characteristics displaying features typical of nonhomogenous material, they make only a small contribution to the thermal transport properties. The thermal conductivity κ is dominated by low- and intermediate-frequency modes.

The majority of the thermal transport in small-grain nanocrystals results from modes delocalized over both GB's and grain interiors. This is apparent in the temperature profiles obtained in the direct heat source and sink simulations shown in Fig. 10. For the amorphous phase and for the d_z=2.7 nm GB structure, the temperature profiles are essentially linear within the statistical noise; i.e., the profile is characteristic of a homogenous materials. However, for the GB structure with a larger d_z of 10.8 nm, the discontinuities in the temperature profile at the GB's are clearly discernible. This indicates that when the grain size increases the picture of heat flow via phonons scattered by GB's is valid. This is further illustrated by the temperature profile of individual GB's (i.e., widely separated) in Fig. 10 which exhibits the most distinct temperature jump ΔT at the GB. This temperature jump arises from a finite interfacial conductance, also known as Kapitza conductance,[30,32] defined as $\sigma_K = J/\Delta T$, where J is the heat flux across the interface.
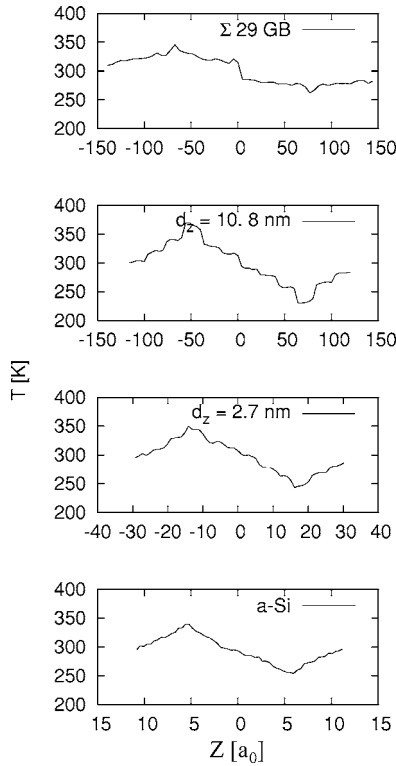
FIG. 10. Comparison of temperature profiles for (A) amorphous silicon, (001) GB structure with (B) $d_z=2.7$ nm, (C) $d_z=10.8$ nm, and (D) individual (001) GB's. The incipience of the temperature discontinuities at GB's is evident in (001) GN structure with $d_z=10.8$ nm.

The effective thermal conductivity was calculated from the average temperature gradients obtained from MD simulations and independently from mode diffusivities and the AF theory [Eq. (7)]. The appropriate quantity to describe thermal transport across interfaces such as grain boundaries is thermal boundary conductance,[32] which is independent of the geometry. Since in our nanocrystalline materials the grain boundaries are the primary source of resistance to thermal transport, in Fig. 11 we plot the ratio of thermal conductivity to the separation between grains, κ/d_z, which we defined as the nominal value of the GB interfacial conductance G_{GB} (Ref. 32). Figure 11 shows G_{GB} as a function of $1/d_z$ at the bottom and d_z at the top of the plot simultaneously. Since the MD simulations are classical, we compare MD with AF calculated with the classical heat capacity.

From Fig. 11, it is evident that for small grain sizes $d_z \lesssim 3$ nm, the thermal conductivities estimated from both methods are quantitatively similar. This demonstrates that the thermal transport properties of nanocrystalline silicon are described well by the harmonic theory of disordered, homogeneous solids in the limit of small grain sizes. This finding is consistent with the polarization analysis (in Sec. IV) in which we observed a shift in the polarization of vibrational modes with increasing grain size from amorphouslike to crystallinelike phonons. For reference, the thermal conductivity of our amorphous structure, $\kappa_{MD} \sim \kappa_{AF} \approx 0.85$ W/m/K.

Increasing the grain size above 3 nm leads to a divergence of the nominal grain-boundary conductance estimates ob-
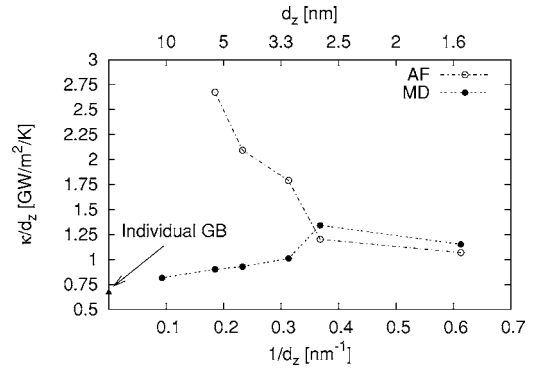

FIG. 11. Thermal conductivity of the (001) GB structures in the direction normal to the GB plane divided by the GB separation, which is the nominal GB conductance, as a function of $1/d_z$. Two data sets are for thermal conductivity obtained in MD simulations and from AF theory. Individual GB conductance is shown at $1/d_z = 0$.

tained from MD simulations and the AF theory of harmonic disordered solids, as illustrated in Fig. 11. In this case the nominal grain-boundary conductance from MD simulations decreases with increasing grain size and tends to a limit of $G_{(001)}=0.67$ GW/m²/K, characterizing individual GB's (i.e., widely separated GB's; see Ref. 30 for more details). By contrast the GB conductance obtained from the AF theory increases, with increasing grain size, clearly demonstrating that in larger-grain-sized nanocrystals, the idea of unpolarized diffusons carrying thermal energy is not applicable. It is not surprising that the AF theory fails in this limit because it is derived under the assumption that the material is homogeneous and hence its thermal properties can be described by a single transport parameter κ. For widely spaced GB's, the interfacial conductance, which is not a bulk property, is clearly important as can be seen from the temperature profiles in Fig. 10. Another important factor is that the AF theory is harmonic and hence does not account for finite phonon lifetimes. In the limit of large grain sizes (i.e., when the grain size begins to be comparable to the mean free path of some phonon modes) it is not reasonable to neglect anharmonic processes entirely.

This crossover, which we documented for the quasi-1D GB structures, is not specific to this geometry or structural model as demonstrated in Fig. 12 which shows a similar transition for 2D textured structures occurring also at a grain size of ~3 nm.

VI. DISCUSSION AND SUMMARY

Our vibrational analysis and results of molecular-dynamics simulations suggest that large-grain-size nanocrystalline materials exhibit a thermal transport mechanism akin to that present in polycrystalline materials. Specifically, the thermal energy is carried by polarized and propagating phonons that are primarily scattered by grain boundaries. With decreasing grain size there is a continuous but distinct crossover in the thermal transport mechanism to diffusive like transport characterizing amorphous and heavily disordered crystalline materials.
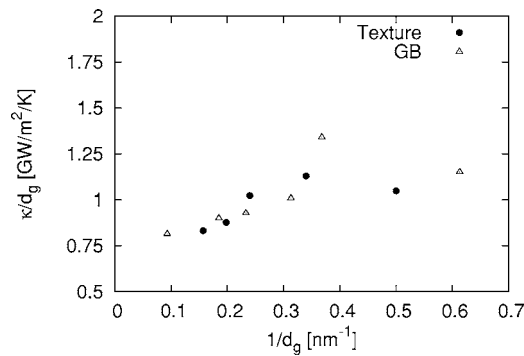
FIG. 12. Thermal conductivity obtained from MD simulations for normal to the GB plane direction for GB superlattices and for in-plane direction for textured 2D microstructures, normalized by the GB separation d_g and plotted as a function of $1/d_g$.

This picture of thermal transport mechanism that emerges from our studies is also consistent with a simple observation that when the wavelengths of the majority of phonons[1] that carry most of the heat are comparable with the grain size, it is no longer reasonable to consider heat as being carried by phonons moving ballistically from one GB to the other and the system can be regarded as homogeneous. Only when the grain size is substantially larger than the wavelength of the majority of phonons do the phonons propagate and scatter in the GB interiors and exhibit discontinuities at GB's and, in turn, invoking a conventional thermal transport mechanism characterizing crystalline materials.

Finally, we discuss the expected temperature dependence of the thermal conductivity of nanocrystalline silicon. For small grain size, we demonstrated that the thermal transport is akin to that present in amorphous silicon;[17,33] therefore, we expect that thermal conductivity will increase and eventually saturate with temperature as is the case for amorphous silicon. This is in contrast to crystalline silicon, which at high temperatures exhibits a decrease of thermal conductivity with increasing temperature due to anharmonicity-mediated umklapp processes.[34] In polycrystalline materials with grain sizes much larger than the bulk of phonon mean free paths, the temperature dependence is the same as that for a perfect crystal. At low temperatures, the mean free path may be larger than the grain size, and then the grain boundaries act as the primary source of thermal resistance. However, in the present studies, even the largest grain sizes of ~10 nm are significantly smaller than the mean free path of acoustic phonons in bulk crystalline silicon.[27,35] Consequently, the thermal conductivity and its temperature dependence are controlled by the GB conductance. The silicon GB conductance was demonstrated to increase modestly with increasing temperature; therefore, we expect that nanocrystalline silicon will exhibit an increase in thermal conductivity with increasing temperature. We would like to point out that such behavior has been reported in experimental studies of nanocrystalline silicon with an average grain size as high as ~200 nm.[35]

In summary, we found that in small-grain-size nanocrystalline structures, the polarization and delocalization features of low- and intermediate-frequency vibrations that carry the most of the heat are similar to those characterizing homogeneous disordered structures, such as amorphous silicon. Increasing the nanocrystalline grain size leads to a gradual increase in the polarization memory and the consequent recognition by the heat-carrying phonons of the inherent structural heterogeneity of the material.

*Electronic address: bodapa@rpi.edu

†Electronic address: keblip@rpi.edu

[1] A. D. McConnell and K. E. Goodson, Annu. Rev. Heat Transfer **14**, 129 (2005).

[2] D. G. Cahill, W. K. Ford, K. E. Goodson, G. D. Mahan, A. Majumdar, H. J. Maris, R. Merlin, and S. R. Phillpot, J. Appl. Phys. **93**, 793 (2005).

[3] D. Gruen, Annu. Rev. Mater. Sci. **29**, 211 (1999).

[4] A. T. Burkov, A. Heinrich, C. Gladun, W. Pitschke, and J. Schumann, Phys. Rev. B **58**, 9644 (1999).

[5] D. M. Rowe, *CRC Handbook of Thermoelectrics: Macro to Nano* (Chemical Rubber, Cleveland, 1995).

[6] G. Soyez, J. A. Eastman, L. J. Thompson, G.-R. Bai, P. M. Baldo, A. W. McCormick, R. J. DiMelfi, A. A. Elmustafa, M. F. Tambwe, and D. S. Stone, Appl. Phys. Lett. **77**, 1155 (2000).

[7] D. Wolf, J. Wang, S. R. Phillpot, and H. Gleiter, Phys. Lett. A **205**, 274 (1995).

[8] S. Veprek, Z. Iqbal, and F. A. Sarott, Philos. Mag. B **45**, 137 (1982).

[9] A. Bodapati, P. K. Schelling, S. R. Phillpot, and P. Keblinski, Appl. Phys. Lett. **88**, 141908 (2006).

[10] J. Callaway, Phys. Rev. **113**, 1046 (1959).

[11] M. G. Holland, Phys. Rev. **132**, 2461 (1963).

[12] J. M. Ziman, *Electrons and Phonons* (Oxford University Press, New York, 1960).

[13] P. Carruthers, Rev. Mod. Phys. **33**, 92 (1961).

[14] R. C. Zeller and R. O. Pohl, Phys. Rev. B **4**, 2029 (1971).

[15] P. W. Anderson, B. I. Halperin, and C. M. Varma, Philos. Mag. **25**, 1 (1972).

[16] W. A. Phillips, J. Low Temp. Phys. **7**, 351 (1972).

[17] J. L. Feldman, M. D. Kluge, P. B. Allen, and F. Wooten, Phys. Rev. B **48**, 12589 (1993).

[18] P. B. Allen and J. L. Feldman, Phys. Rev. B **48**, 12581 (1993).

[19] P. B. Allen, J. L. Feldman, J. Fabian, and F. Wooten, Philos. Mag. B **79**, 1715 (1999).

[20] F. H. Stillinger and T. A. Weber, Phys. Rev. B **31**, 5262 (1985).

[21] P. Keblinski, D. Wolf, S. R. Phillpot, and H. Gleiter, J. Mater. Res. **13**, 2077 (1998).

[22] J. Q. Broughton and X. P. Li, Phys. Rev. B **35**, 9120 (1987).

[23] P. Keblinski, S. R. Phillpot, D. Wolf, and H. Gleiter, J. Am. Ce-

ram. Soc. **80**, 717 (1997).

[24] P. Jund and R. Jullien, Phys. Rev. B **59**, 13707 (1999).

[25] P. K. Schelling, S. R. Phillpot, and P. Keblinski, Phys. Rev. B **65**, 144306 (2002).

[26] A. Maiti, G. D. Mahan, and S. T. Pantelides, Solid State Commun. **102**, 517 (1997).

[27] P. K. Schelling, S. R. Phillpot, and P. Keblinski, J. Appl. Phys. **95**, 6082 (2004).

[28] J. L. Feldman and N. Bernstein, Phys. Rev. B **70**, 235214 (2004).

[29] P. M. Derlet, R. Meyer, L. J. Lewis, U. Stuhr, and H. Van Swygenhoven, Phys. Rev. Lett. **87**, 205501 (2001).

[30] P. K. Schelling and S. R. Phillpot, J. Am. Ceram. Soc. **84**, 2997 (2001).

[31] R. J. Bell and P. Dean, Discuss. Faraday Soc. **50**, 55 (1970).

[32] E. T. Swartz and R. O. Pohl, Rev. Mod. Phys. **61**, 605 (1989).

[33] D. G. Cahill and R. O. Pohl, Phys. Rev. B **35**, 4067 (1987).

[34] C. J. Glassbrenner and G. A. Slack, Phys. Rev. **134**, A1058 (1964).

[35] S. Uma, A. D. McConnell, M. Ashegi, K. Kurbayashi, and K. E. Goodson, Int. J. Thermophys. **22**, 605 (2001).